Organ Localization:

Moving Toward Patient Specific Prospective Organ Dosimetry for CT

by

Kevin F. Rybicki

Graduate Program in Medical Physics
Duke University

Date:_____

Approved:

_____
W. Paul Segars, Supervisor

_____
Ehsan Samei, Chair

_____
Terence Z. Wong

Thesis submitted in partial fulfillment
of the requirements for the degree of Master of Science in the
Graduate Program in Medical Physics in the Graduate School
of Duke University

2012

ABSTRACT

Organ Localization:

Moving Toward Patient Specific Prospective Organ Dosimetry for CT

by

Kevin F. Rybicki

Graduate Program in Medical Physics
Duke University

Date:_____

Approved:

_____
W. Paul Segars, Supervisor

_____
Ehsan Samei, Chair

_____
Terence Z. Wong

An abstract of a thesis submitted in partial
fulfillment of the requirements for the degree
of Master of Science in the Graduate Program in
Medical Physics in the Graduate School
of Duke University

2012

Abstract

Purpose: Radiation doses from computed tomography (CT) examinations have come under public and governmental scrutiny because of several recent misadministrations of radiation across the country. Current CT dosimetry methods in the clinic use standardized cylindrical water phantoms to measure radiation dose across various scanning protocols and different scanner manufacturers. These methods and equipment are too generalized to provide accurate risk assessment for patients of varying ages, genders, and anatomies. The advent of computer models based on real CT imaged anatomy has made patient specific and organ specific dosimetry achievable.

With a population of both pediatric and adult patient models comprised of a wide range of anatomies, Monte Carlo based dose calculations can be cataloged. A patient can receive a prospective dose estimation from a phantom within our population that best exhibits the patient's age and anatomical characteristics. Knowledge of organ size and location is essential to finding a proper match between the patient and the computer model. To this end, very little information is currently available regarding organ size and location across a diverse human population. The purpose of this study was to develop a predictive model to ascertain organ locations and volumes for pediatric and adult patients.

Methods: This study included 51 adults and 40 pediatrics from which Extended NURBS-based Cardiac-Torso (XCAT) phantoms were generated. Large organs were manually segmented from clinical CT data. The remaining organs and other anatomical structures were created by transforming an existing human model template to fit the framework of the segmented structures. The maximum and minimum points of the organs were recorded with respect to the axial distance from the tip of the sacrum. The axial width and midpoint for each organ were then determined. The organ volumes were also calculated. All three organ parameters were plotted as functions of patient age and weight for adults and patient age for pediatrics.

Results: The adult patients showed no statistically significant correlation between organ parameters and patient age and BMI. There were slight, positive linear trends with organ midpoint (max r^2=0.365, mean r^2=0.185) and organ volume (max r^2=0.510, mean r^2=0.183) versus adult patient weight. The height correlations were also positive for midpoint (max r^2=0.485, mean r^2=0.271) and volume (max r^2=0.475, mean r^2=0.206) Gaussian fits performed on probability density functions of adult organs resulted in r^2-values ranging from 0.945 to 0.996. Pediatric patients demonstrated strong cube root relationships with organ midpoints (max r^2=0.857, mean r^2=0.790) and organ widths (max r^2=0.905 , mean r^2=0.564) versus age. Pediatric organ volumes showed positive linear relationships versus age (max r^2=0.983, mean r^2=0.701).

Conclusions: Adult patients exhibited small variations in organ volume and location with respect to weight and height, but no meaningful correlation existed between these parameters and age or BMI. Once adulthood is reached, organ morphology and positioning seems to remain static; however, clear trends are evident between pediatric age and organ volumes and locations. Such information can aid in the selection of an appropriate computer model that has the highest probability of mirroring the anatomy of a patient undergoing a clinical exam.

Dedication

For my mother, who at the time of this publication is concluding a 7 year long battle with cancer.

Contents

List of Tables

List of Figures

Acknowledgements

This work would not be possible without the guidance and support from my research advisors Paul Segars and Ehsan Samei, who gave me the opportunity to complete this project when the odds were against me. To my friends and classmates here at Duke: sharing the ups and downs of these 2 years has helped shape me into the physicist and the person I am today. To Kate: your unwavering love and belief in me have helped me achieve things I could have never done on my own. To my family: thank you for the love that has guided me through the difficult times and allowed me to experience continued success. And finally, to my mother: I will carry your kindness and warmth in my heart for as long as I live. Your struggles have given me the strength and courage to overcome the obstacles in my life. I love you.

1. Introduction

1.1 Radiation Risk in Clinical Exams

The use of radiation in medical imaging is a double-edged sword: on the one hand, radiation is the source of diagnostic power for many modalities. Bombarding anatomical structures with photons is the essential process of image formation in radiography and computed tomography (CT). On the other hand, those same photons that allow clinicians to diagnose disease carry the risk of cancer induction. The primary responsibility of the imaging physicist is to enhance diagnostic power while minimizing risk to the patient [1].

For the better part of the 20th century, radiography dominated the medical imaging world as the primary modality. With the advent of computers and the arrival of CT in the 1970s, the limitations of radiography became more apparent. CT provided a method to remove the overlapping structures that obscure vital information in radiography. Radiologists were no longer limited to a two-dimensional projection but could see slices of three-dimensional data. With that enhanced resolution, however, comes greater dose to the patient. Even with increasingly sophisticated techniques, CT does not change the underlying physics of x-ray imaging. The dichotomy of image quality versus patient dose still stands as the central problem for imaging physicists. And as the technology becomes more and more complex, so too does the problem of risk assessment. Table 1 compares doses from various pediatric exams relative to a typical

chest radiograph. By these estimations, CT effective doses are two orders of magnitude greater than that of a conventional chest x-ray. It should be noted that effective dose is not a measure of absolute dose but rather an equivalent whole body dose. Still, this is a clear indication that the medical community must make strides in monitoring and regulating CT dose.

Table 1: Estimated effective doses and equivalent chest radiographs (CXR) for various exams for a 5 year old child. CT scans are shown in bold [2].

Imaging Area	Effective Dose (mSv)	Equivalent # of CXRs
3-view ankle	0.0015	1/14
2-view chest	0.02	1
AP and lateral abdomen	0.05	2.5
Tc-99m cystogram	0.18	9
Tc-99m bone scan	6.2	310
FDG PET scan	15.3	765
Fluoroscopic cystogram	0.33	16
Head CT	**4.0**	**200**
Chest CT	**3.0**	**150**
Abdomen CT	**5.0**	**250**

1.2 Spread of CT into Mainstream Clinical Use

In 1993, there were approximately 18.3 million CT scans done in the United States alone. The most recent National Council on Radiation Protection and Measurements (NCRP) publications report an estimated 62 million scans done in 2006. Over that 13-year period there was an average increase of roughly 10% per year [3].

Even a conservative estimate would predict the number of CT procedures carried on in 2012 to be well over 90 million. The introduction of mutidetector CT (MDCT) and increased computing power have expanded the clinical use of CT scans. With wider field of views and faster reconstruction, cardiac and respiratory gated acquisitions give CT the power of temporal resolution and a whole new array of applications.

To put these numbers in perspective, the 63 million CT scans in 2006 were less than half the number of chest radiographs—128 million—done in that same year. But as discussed in Section 1.1, the dose contribution from CT far exceeds that of a chest radiograph. Figure 1 shows the annual dose contribution for patients in the US from medical procedures.

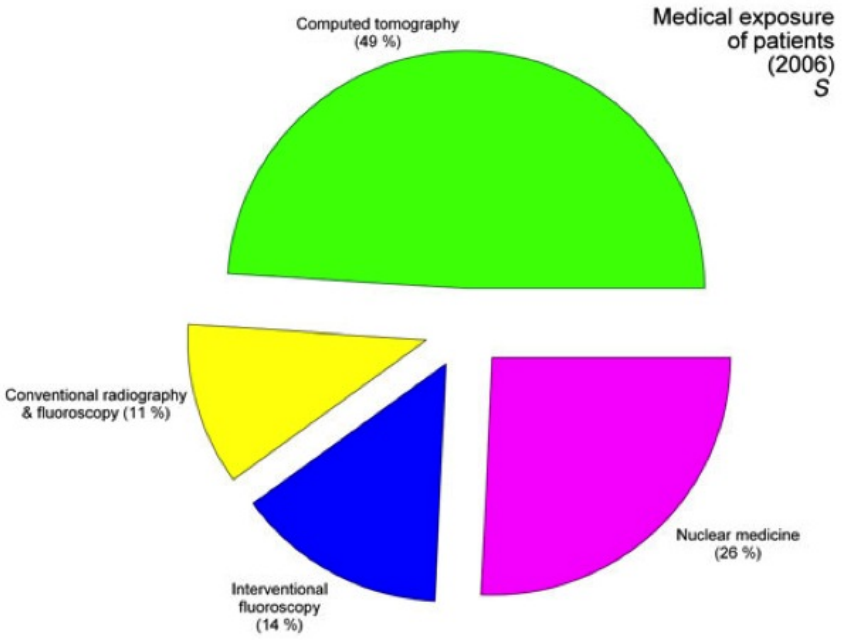

Figure 1: Percent contribution to the annual effective dose for the US population from medical exposures. Notice how the CT contribution (49%) far exceeds the conventional radiography/fluoroscopy portion (11%) [3].

With nearly half of the radiation dose to patients attributed to CT, dose measurement and risk assessment in computed tomography becomes a vitally important issue for the diagnostic physicist to address. Along with the widespread use of CT comes an abundance of negative media attention due to CT related accidents in hospitals across the country [4-5]. This heightened public awareness increases the need for stricter regulatory control of medical radiation.

1.3 Current CT Dosimetry Methods

In August 2010, the California state legislature passed Senate Bill 1237 due in large part to the documented misadministrations in CT exams. SB 1237 outlines regulations for dose reporting, facility accreditation, and medical event reporting to ensure public safety. Commencing July 1, 2012, California hospitals will be required to report the Computed Tomography Volume Dose Index ($CTDI_{vol}$) and Dose-Length Product (DLP) for each CT exam conducted [6].

This marks the first government efforts to manage and monitor patient dose in CT exams. And while this is a good first step toward that goal, the two parameters—$CTDI_{vol}$ and DLP—have serious limitations when applied to individual patients and exams. It is the responsibility of diagnostic physicists to understand these concepts and advise the implementation of appropriate methods of dose monitoring in their institution.

1.3.1 Origins of the $CTDI_{vol}$ and DLP

In 1991, the American Association of Physicists in Medicine (AAPM) introduced standardized methods for the measurement of CTDI. CDTI is used to provide a dose comparison between different machine settings and different scanner manufacturers. A 16 cm diameter cylindrical head phantom and 32 cm diameter body phantom with equally spaced ion chambers are placed on the patient table for dose estimation. Figure 2 shows a schematic of the tissue equivalent head phantom [7].

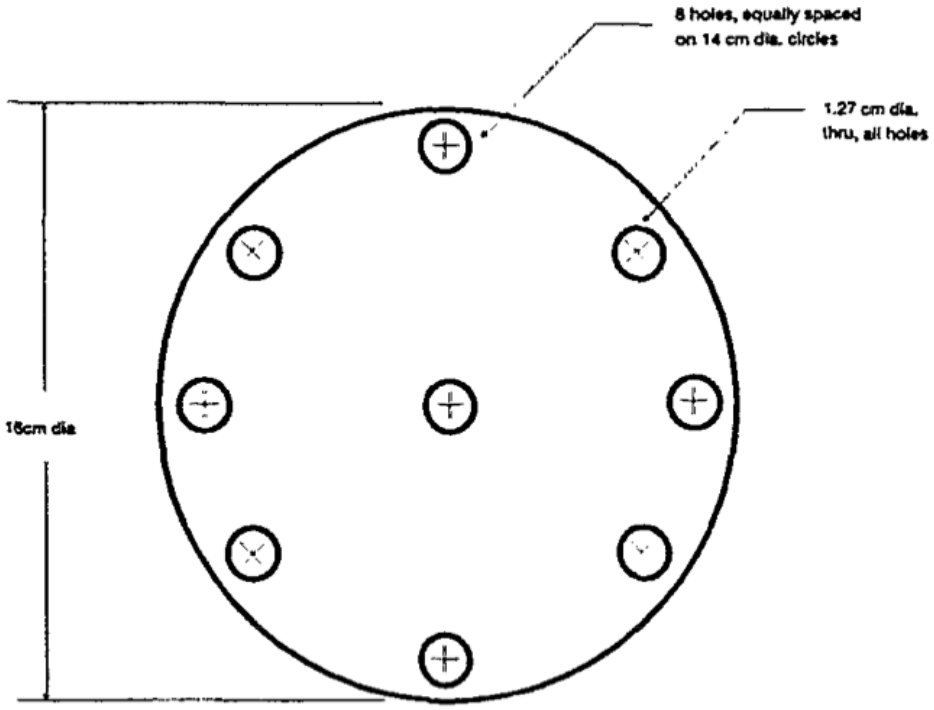

Figure 2: CT head phantom schematic taken from the 1991 AAPM Report No. 31. This continues to be the primary standard for measuring dose indices.

The AAPM Report No. 96 published in 2008 outlined several new indices related to the 1991 CTDI. The $CTDI_{FDA}$, $CTDI_{100}$, $CTDI_{W}$, $CTDI_{vol}$, and DLP were each introduced

to resolve problems that arose with their predecessors [8]. All these parameters, however, have one thing in common: the cylindrical water phantoms used to make the dose measurements.

1.3.2 New Dosimetry Metrics

With a single pair of cylinders it is impossible to represent an entire population of adult and pediatric anatomies. While a single standardized phantom has the benefit of widespread availability to institutions and simple measurement procedures, increased sophistication is needed to yield more accurate and meaningful dose estimates.

To this end, two new methodologies have surfaced. The first, outlined by the AAPM Task Group 111 in February 2011, calls for replacing the CTDI model with a new metric called the "equilibrium dose" D_{eq}. This method provides more accurate modeling of primary and scattered radiation. [9]. The equilibrium dose is still in the early stages of formulation and standards on phantoms and measurement protocols have yet to be established.

The second method, size specific dose estimation (SSDE), aims to keep the CTDI convention in place while establishing size dependent coefficients to correct the $CTDI_{vol}$ and DLP for patient size [10]. The work of Zhang *et al.* compares the variation of CTDI as measured in anthropomorphic phantoms with the conventional CTDI cylindrical phantom [11]. Other studies examine cylindrical phantoms of varying diameter and

plot the change in CTDI [12]. Further advancements have been made to track individual organ dose as a function of chest diameter [13].

1.4 Organ Localization and Prospective Dosimetry

Ever since x-ray tube current modulation came into clinical practice, there has been a need for a more nuanced approach to risk assessment for CT examinations. As the patient table travels through the bore, the tube current adjusts to the patient thickness. This current modulation is recorded both radially and axially. Knowing the size and location of the patient's organs would allow for precise dose calculations. This can be done retrospectively, after the examination is over. With the CT images, the organ locations are exactly known, and dose can be calculated from the tube current modulation data.

To do this for every patient that walks through the door would be impossibly tedious and impractical. The aim of this study is to examine the size and location of radiosensitive organs in the torso over a wide spectrum of patient ages and anatomies. By building a database of organ coordinates and volumes, the dose calculations and risk assessments can be done ahead of time. A patient coming in for a CT scan can be assigned to a particular cohort that best represents his/her anatomy and be given a prospective dosimetry assessment for each of organ.

At the time of this study, there has been little consideration given to patient specific organ volumetry. The work of Breiman *et al*. examines canine kidney volumes

and human spleen volumes [14]. Others have also studied splenic volumes for adult populations and their correlation to height [15-16]. The liver volume has also been measured using CT and sonography [17-18]. The spleen and liver are of particular interest to physicians because deviations in volume can indicate blood pathologies. From a dosimetry standpoint, however, the volume and location of all radiosensitive organs are important for estimating organ dose and patient risk.

Building upon the XCAT models currently under development at our institution, this specific project examines location along the axial direction as a first order approximation of organ localization. Dependencies on patient age, weight, height, and body mass index (BMI) are examined to determine the most prominent relationships. Organ volumes are treated in a similar fashion. The data is used to develop a predictive model by which organ location can be ascertained for a given individual. It is expected that that these models can be incorporated with dosimetry techniques to determine patient and organ dose in such a way that they are patient specific.

2. Materials and Methods

2.1 XCAT Phantoms

As described in Sections 1.3.1, the current clinical dosimetry efforts are measured on uniform cylindrical phantoms. While these materials are widely accessible to institutions, they limit the accuracy of dose estimation, especially for pediatric patients. More recent efforts have utilized pediatric anthropomorphic phantoms. This is in an improvement over the conventional 16 cm and 32 cm cylinder phantoms, however, the phantoms are built for discrete ages (1, 5, and 10 years) and fail to provide patient specific information [19]. Through the work of Segars *et al.*, extended 4D NURBS-based Cardiac-Torso (XCAT) phantoms have been developed to bring new levels of detail and flexibility to imaging analysis and optimization. These computerized human models are built from real patient anatomy, ranging from newborns to adults {20}. Below we describe a summary of how the current XCAT models are developed.

2.1.1 Patient Data Acquisition and Organ Segmentation

The CT datasets are obtained from the Duke University Medical System. The cohort used in this study includde 51 adults and 40 pediatrics. The adult patients ranged from 18 years to 78 years with a mean age of 52 years. The pediatric patients ranged from 5 weeks to 15 years with a mean age of 5 years. Figure 3 shows the uniform age distribution of the CT datasets. All CT examinations were reviewed by an

experienced pediatric radiologist to ensure that they represent normal anatomy, i.e. contain no pathologies that would affect organ size, location, or morphology.

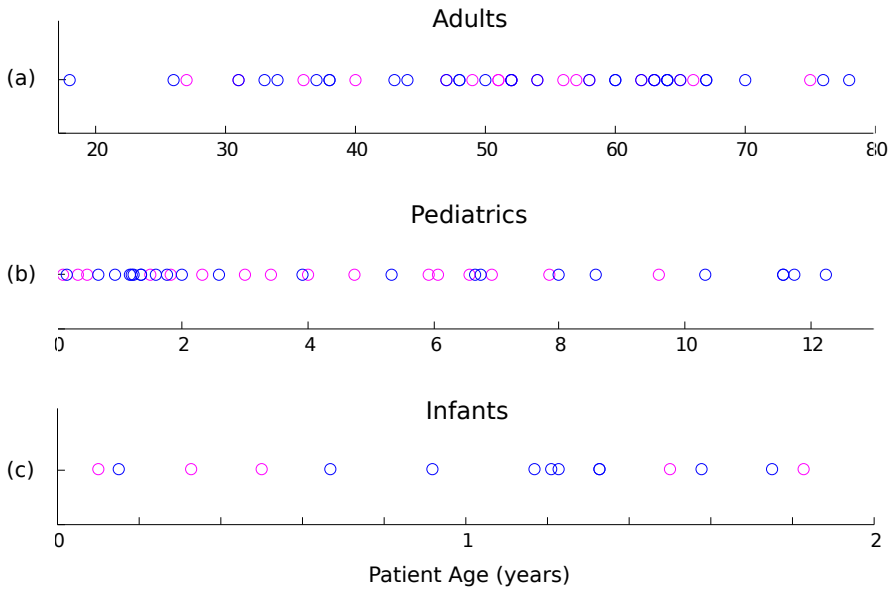

Figure 3: Age distributions for (a) adult patients, (b) all pediatric patients, and (c) infant patients. Males are shown in blue and females in pink. Figure 3c is a subset of Figure 3b.

For the adult datasets, major organs and anatomical structures are manually segmented. These structures include: vertebrae, clavicle, ribs, ischium, sacrum, lungs, heart, liver, spleen, stomach, kidneys, gall bladder, pancreas, breasts, thyroid, and body outlie. The same structures are contoured for the pediatrics with the exception of the thyroid. Figure 4 displays the Graphical User Interface (GUI) used to segment the patient data.

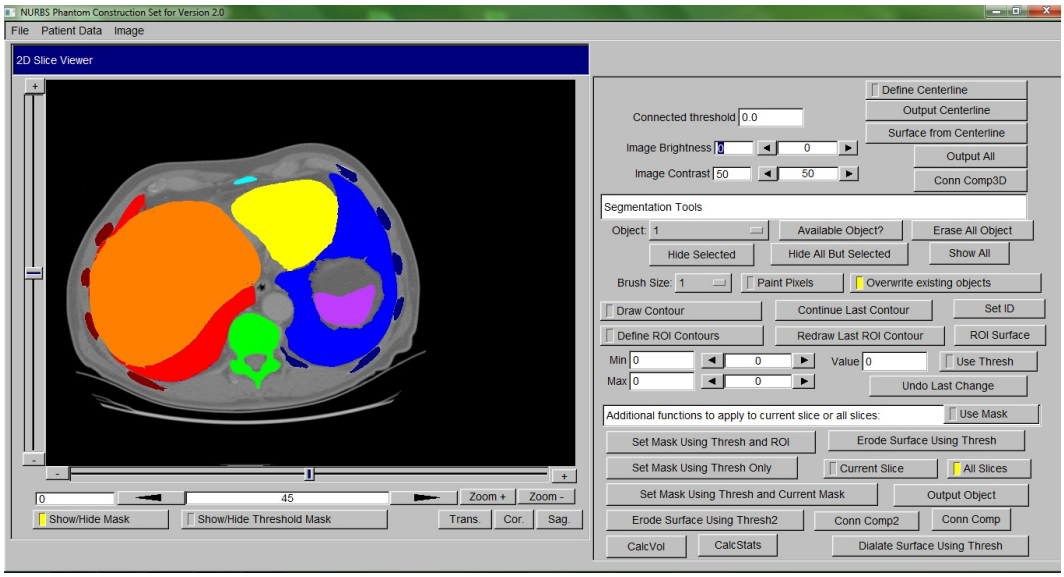

Figure 4: GUI used for segmenting organs from patient CT data. Each color corresponds to a different organ mask [20].

The resulting 3D polygon models created for each organ are then imported into Rhinoceros, a non-uniform rational B-spline (NURBS) modeling program. This takes the segmented organ data and creates a NURBS surface, a meshed surface contour. Whereas voxelized models are static, NURBS based models have mathematically defined surfaces that can be manipulated to simulate cardiac and respiratory motion. Each transaxial CT image has a thickness corresponding to the axial resolution of the scan (typically 5mm). Thus the organ volumes are appropriately scaled by this factor for each patient.

2.1.2 LDDMM Transform

The anatomical structures listed in Section 2.1.1 represent only a small portion of the more than 9000 surfaces found in a complete XCAT phantom (see Figure 5). The

heads, extremities, and any incomplete organs were manually added in Rhinoceros using a completed XCAT model as a template. The template was chosen to match the patient age, gender, and size as closely as possible. Any sharp edges in the segmented organs were smoothed out as well.

To complete the rest of the human model, the Large Deformation Diffeomorphic Metric Mapping (LDDMM) framework developed at Johns Hopkins was used [21]. The LDDMM algorithm is a non-rigid, high-dimensional transformation requiring a template image and a target image. The transformation has a one to one correspondence of template points to target points. Voxelized versions of the incomplete models were generated to serve as the targets. An existing XCAT phantom was voxelized to serve as the template. The LDDMM algorithm calculates a mathematical transform to map the template images to the target images. This relationship was solely based on transforming the structures that were manually contoured from real patient data, which was then applied to the rest of the anatomy to complete the target model. The feasibility of these methods has been verified against International Commission on Radiological Protection (ICRP) anatomical values and voxelized phantoms from the University of Florida [20].

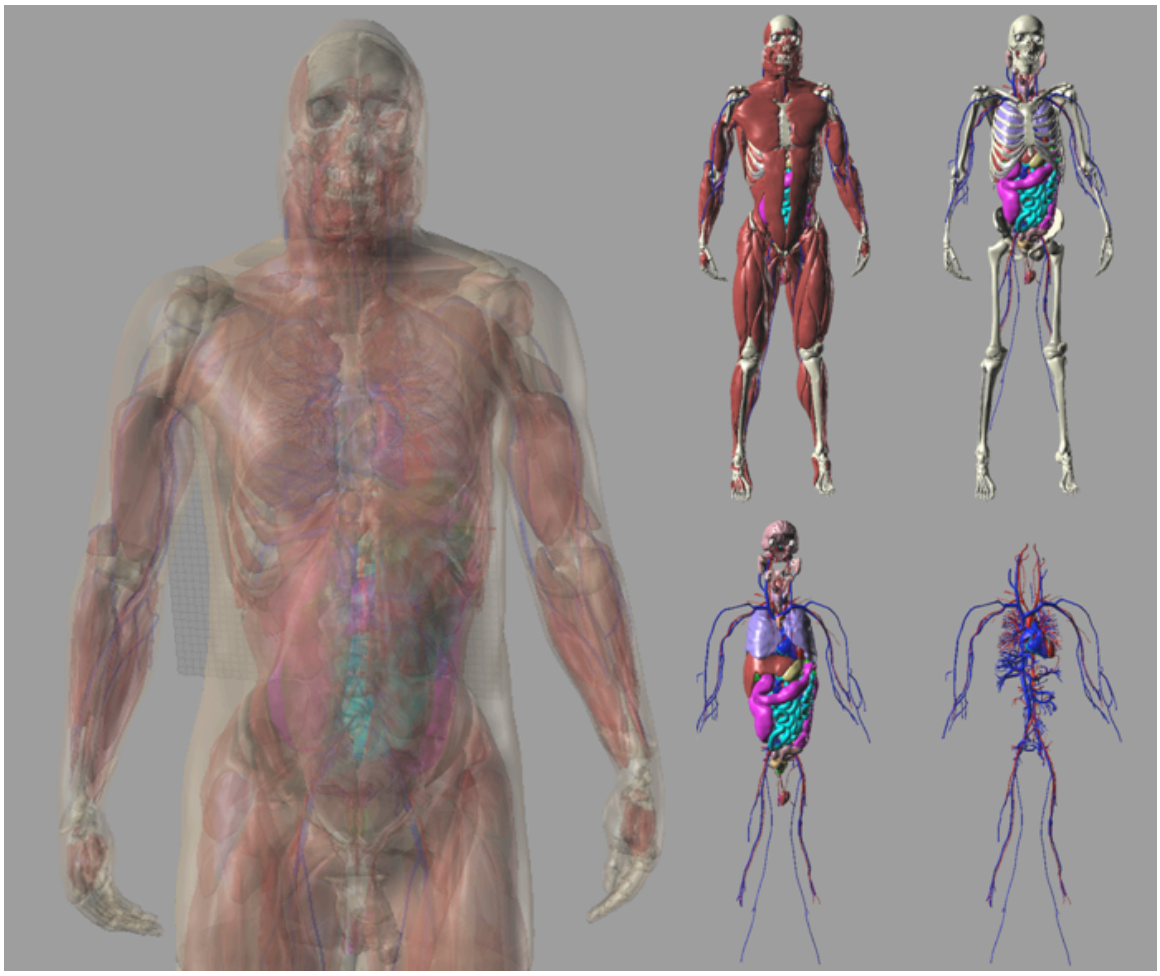

Figure 5: Complete male XCAT phantom (left). At right, progression of model detail showing vasculature, organs, skeleton, and muscles [20].

2.2 Organ Localization

As described in Section 2.1.1, the manually segmented organs are imported into Rhinoceros as 3D polygon surfaces. By projecting the surface onto the sagittal (X), coronal (Y), and axial (Z) planes, a rectangular volume can be formed to localize the organ as in Figure 6. The coordinate system was defined with 0.1 mm precision with the tip of the sacrum designated as the origin.

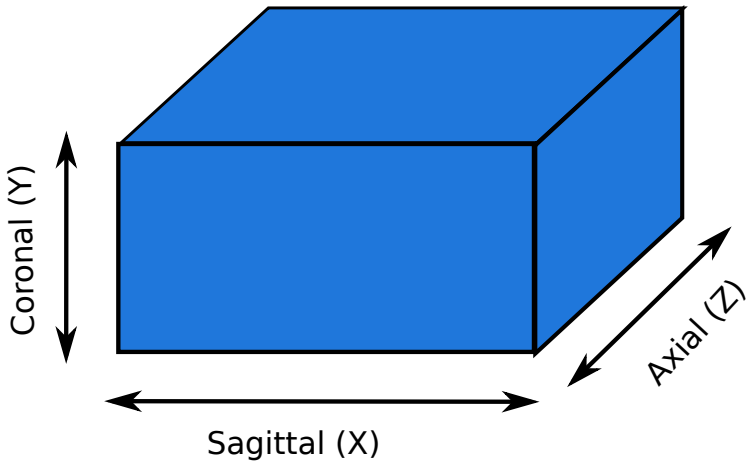

Figure 6: Coordinate axes defined for rectangular organ volume

To accurately localize an organ, both the organ size and location must be considered. The minimum and maximum values of all three axes were recorded for each organ. The x, y, and z widths were calculated as the difference between the respective maximum and minimum values. The midpoints were similarly defined as the average of the maximum and minimum points.

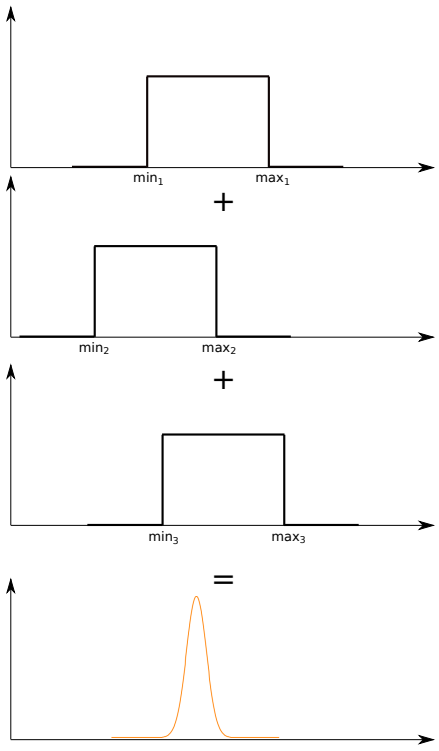

Figure 7: Summation of overlapping 1D rect functions to form an organ probability density function

For the adult models, one-dimensional rect functions were constructed from the minimum and maximum points for each organ. This effectively combines the organ width and location into a single metric. A probability density function (PDF) was created from normalizing the sum of overlapping rect functions and fitted with a Gaussian curve (see Figure 7). The fit was performed with a non-normalized Gaussian function

$$f(x) = a \ \ exp\left[-\frac{(x-\mu)^2}{2\sigma^2}\right], \tag{1}$$

where a is the amplitude, μ is the mean, and σ is the standard deviation. In instances where the fit resulted in a Gaussian with a frequency amplitude greater than 1.0, the amplitude was normalized to 1.0 and the r^2-values were calculated. These normalized organs are boldfaced and italicized in Table 4. The bladder was ignored in this analysis since it varies greatly from patient to patient. A few transformed (i.e. not manually segmented) organs were included to compare with the manually segmented data (denoted with an asterisk in the data tables). With Gaussians fitted to the PDFs, normal distribution statistics were used to establish 95% confidence boundaries in the axial direction within $\pm 2\sigma$ of the mean.

Both the adult and pediatric datasets were also fitted by three different functions: lines, logarithms, and cube roots. The cube root functions followed the form

$$f(x) = a\sqrt[3]{x} + b\ . \tag{2}$$

Organ volumes were measured for both cohorts. The splenic volumes were compared with existing data.

3. Results

3.1 Adults

3.1.1 Axial Midpoint

The adult models showed no correlation between organ axial midpoint and patient age or BMI and thus were most effectively analyzed as a single cohort using probability distribution functions (Section 3.1.3). Weak linear trends were seen between axial midpoint and patient weight: as patient weight increases, axial midpoint increases (as defined from the sacrum). The heart demonstrates the strongest of these positive linear trends with weight. The lungs show the strongest correlation with patient height. The mean r^2-value for weight is 0.185 and for height is 0.271. Plots for the heart, liver, and spleen are shown in Figure 8. The plots demonstrate a random distribution of midpoints when plotted versus age. By comparison, the right column indicates that there is some linear relationship between axial midpoints and weight. The slopes of the linear fits, r^2-values, and mean midpoints are listed in Table 2.

Table 2: Linear fit data for axial midpoint versus patient weight and height demonstrating slight positive relationships. Organs that were not manually segmented are marked with an asterisk

Organ:	Slope - Wt	r^2 - Wt	Slope - Ht	r^2- Ht	Mean Midpoint (mm)
Left Adrenal*	0.263	0.060	0.942	0.150	292.1
Right Adrenal*	0.326	0.063	1.657	0.318	295.5
Gall Bladder	0.785	0.232	1.429	0.149	272.7
Heart	0.889	0.365	1.721	0.267	409.1
Left Kidney	0.149	0.021	0.759	0.104	257.6
Right Kidney	0.172	0.022	1.28	0.237	247.5
Liver	0.656	0.226	1.271	0.165	299.9
Left Lung	0.652	0.203	2.187	0.446	447.1
Right Lung	0.587	0.182	2.169	0.485	444.7
Pancreas	0.608	0.200	1.324	0.185	281.7
Spleen	0.667	0.281	1.103	0.131	315.6
Stomach	0.907	0.357	1.792	0.214	315.5
Thymus*	0.967	0.184	2.061	0.317	476.1
Thyroid	0.698	0.060	2.917	0.628	584.9

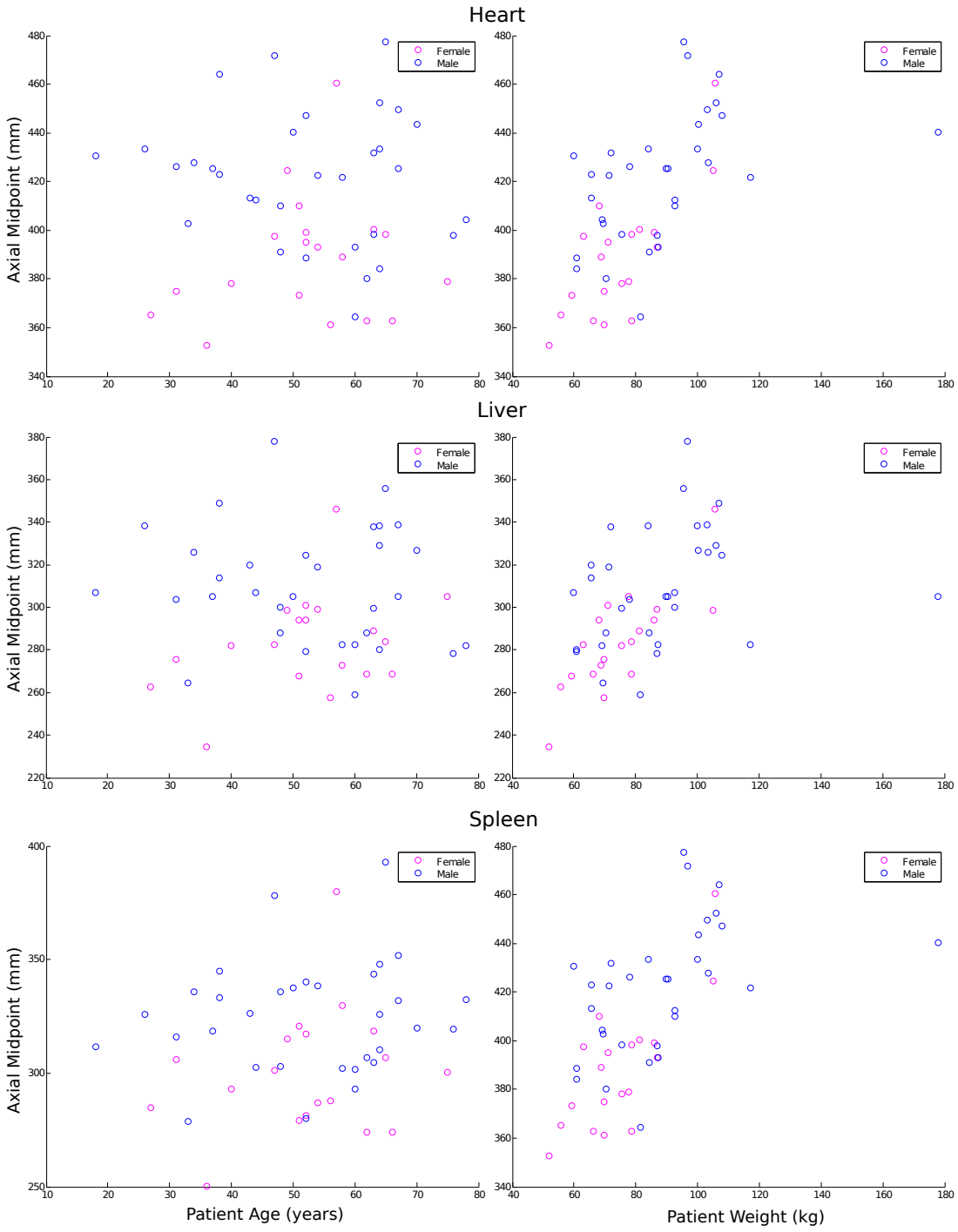

Figure 8: Midpoints of heart, liver, and spleen each plotted against patient age and weight. Patient weight exhibits a weakly positive correlation to axial midpoint location while patient age shows virtually no correlation.

3.1.2 Axial Width

The axial width of the organs exhibited behavior similar to that of the organ midpoints. There is no meaningful relationship between patient age and BMI and organ width. The correlation between axial width and patient weight is slightly linear, albeit to a lesser extent than the organ midpoints (weight mean $r^2 = 0.055$ and height mean $r^2 = 0.117$). We see the highest correlations between the liver and spleen with weight and the lungs with height. Table 3 shows the slopes and r^2-values for the linear fits performed and the mean organ widths. The r^2-values are much smaller than the ones found in Table 2, indicating a less significant linear behavior.

Table 3: Linear fit data for axial width versus patient weight demonstrating a slight linearity. Organs that were not manually segmented are marked with an asterisk.

Organ:	Slope - Wt	r^2 - Wt	Slope - Ht	r^2 - Ht	Mean Width (mm)
Left Adrenal*	-0.070	0.017	0.037	0.002	48.8
Right Adrenal*	0.058	0.020	0.269	0.085	45.5
Gall Bladder	-0.070	0.017	0.210	0.029	42.9
Heart	0.068	0.029	0.358	0.162	110.5
Left Kidney	0.148	0.097	0.320	0.088	101.9
Right Kidney	0.139	0.070	0.401	0.114	97.7
Liver	0.360	0.147	0.568	0.071	166.6
Left Lung	-0.010	0.000	1.625	0.342	229.8
Right Lung	0.121	0.009	1.673	0.321	230.0
Pancreas	0.015	0.000	0.310	0.023	75.8
Spleen	0.287	0.117	0.689	0.132	85.8
Stomach	-0.378	0.107	-0.084	0.001	89.2
Thymus*	0.123	0.039	0.613	0.189	81.4
Thyroid	-0.125	0.102	0.259	0.085	63.8

3.1.3 Organ PDFs

The organ PDFs match very closely with Gaussian functions with a mean r^2-value of 0.981 (see Figures 9-11). The liver and lung PDFs generated Gaussians with amplitudes greater than 1.0. These PDFs have plateaus with frequency equal to 1.0 in areas where all 51 patient rect functions coincided. Since a frequency greater than 1.0 makes no physical sense, they were refitted with Gaussians manually set with $a = 1.0$. Figure 10 shows the Gaussian function extending beyond the boundaries of the measured PDF. Table 4 lists the mean, standard deviation, r^2-value, and 95% confidence interval for each organ.

Table 4: Summary of Gaussian fit statistics. Mean, standard deviation, and 95% confidence intervals are expressed in millimeters. The liver and lungs are fitted with Gaussians with amplitudes normalized to 1.0. Organs that were not manually segmented are marked with an asterisk.

Organ:	r^2	Mean (μ)	SD (σ)	95% min	95% max	95% width
Left Adrenal*	0.992	289.3	25.5	238.3	340.2	101.9
Right Adrenal*	0.978	294.3	32.7	229.0	359.7	130.7
Gall Bladder	0.974	265.6	31.2	203.1	328.0	124.8
Heart	0.996	408.2	47.3	313.7	502.8	189.1
Left Kidney	0.980	255.9	41.5	172.8	339.0	166.2
Right Kidney	0.993	246.5	40.5	165.6	327.4	161.9
Liver	0.978	299.1	66.4	166.2	432.0	265.8
Left Lung	0.948	446.8	90.9	265.1	628.5	363.4
Right Lung	0.945	444.3	90.9	262.5	626.1	363.5
Pancreas	0.993	278.7	37.2	204.3	353.0	148.7
Salivary Gland*	0.993	683.3	50.1	583.1	783.5	200.4
Spleen	0.994	314.2	39.3	235.7	392.7	157.0
Stomach	0.993	312.0	46.1	219.7	404.3	184.6
Thymus*	0.995	476.4	44.3	387.8	564.9	177.1
Thyroid	0.980	589.0	41.0	507.1	671.0	163.9

The r^2-values signify a very high correlation between the fits and the measured distributions. This validates the use of normal distribution statistics to determine a 95% confidence interval within 2σ of the mean.

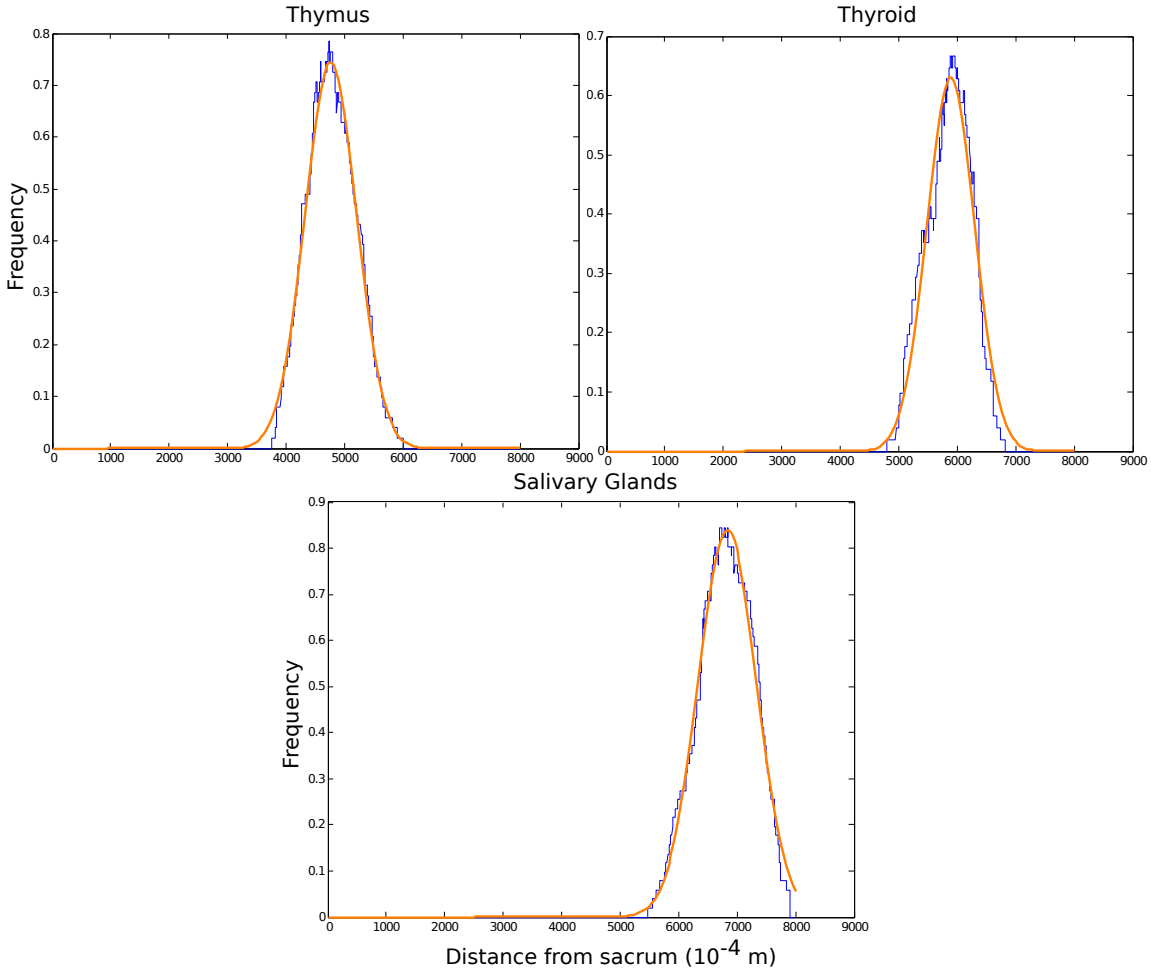

Figure 9: Probability density functions (blue) with Gaussian fits (orange) for the thymus, thyroid, and salivary glands.

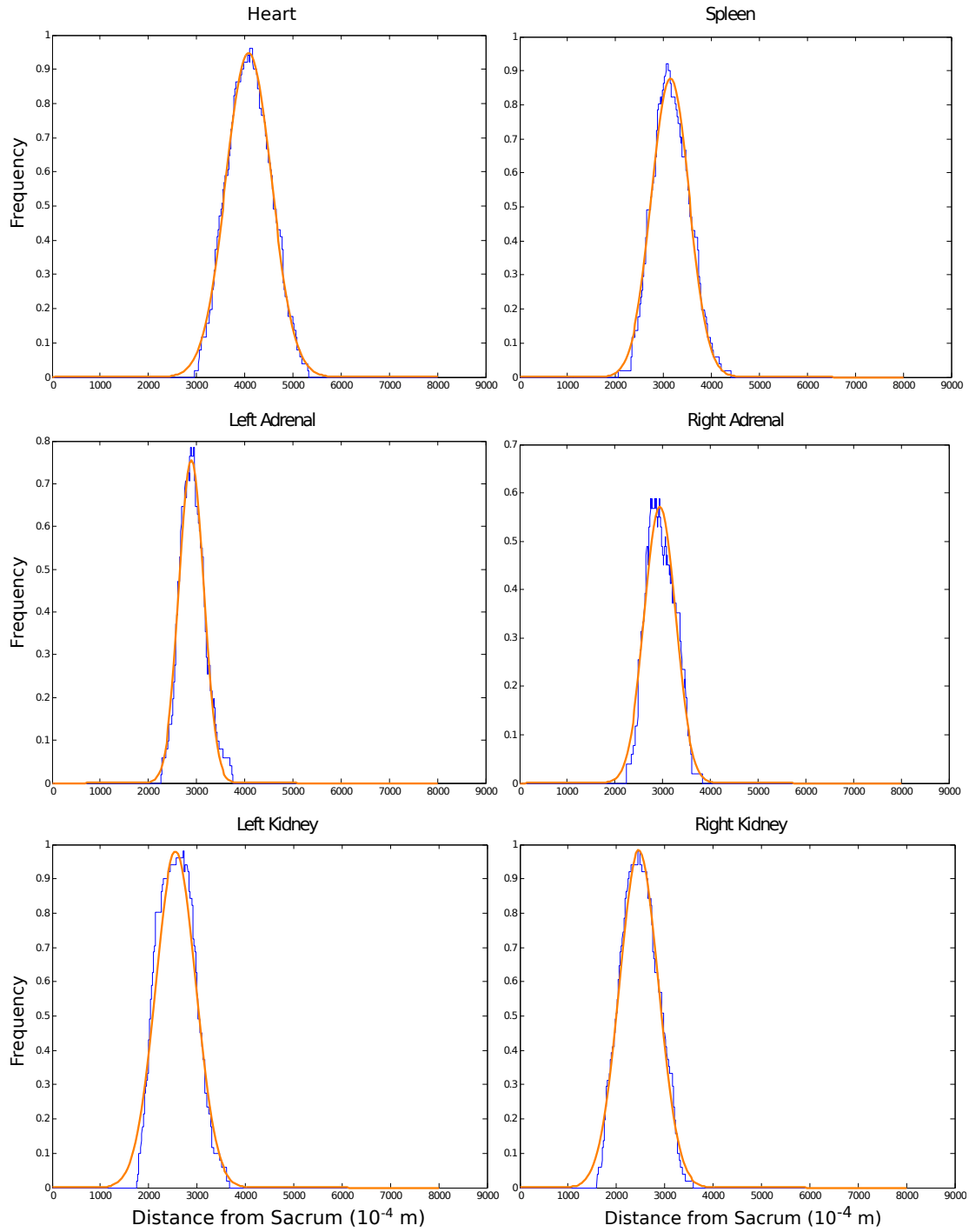

Figure 10: Probability density functions (blue) with Gaussian fits (orange) for the heart, spleen, left and right adrenal glands, and left and right kidneys.

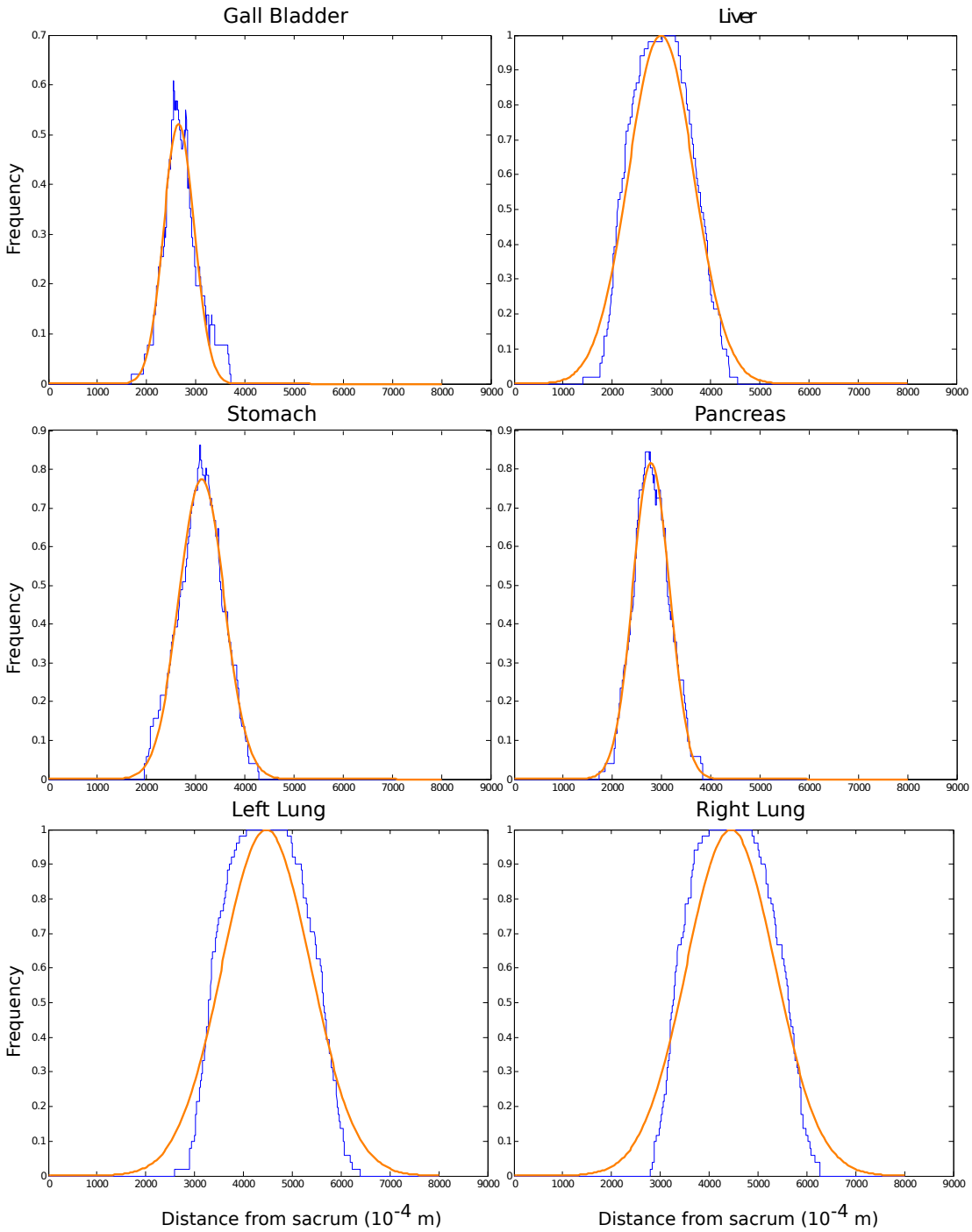

Figure 11: Probability density functions (blue) with Gaussian fits (orange) for the gall bladder, liver, stomach, pancreas, and left and right lungs.

3.1.4 Organ Volume

The organ volumes share similar trends with the axial widths and midpoints in that there is no discernable correlation between age and BMI with organ volume for adults (see Figure 12). Table 5 summarizes the relationship between organ volume and patient weight. The r^2-values indicate a more significant positive, linear correlation with weight for the kidneys and liver than any other organ. Similarly, the highest r^2-values for patient height correspond to the lungs.

Table 5: Summary of linear fit data for organ volume as a function of patient weight and height. The mean volumes are reported in units of cubic centimeters. Organs that were not manually segmented are marked with an asterisk.

Organ	Slope - Wt	r^2 - Wt	Slope - Ht	r^2 - Ht	Mean Volume (cm^3)
Left Adrenal*	0.005	0.022	0.022	0.078	7.2
Right Adrenal*	0.007	0.046	0.029	0.135	7.6
Gall Bladder	0.302	0.098	0.554	0.063	31.2
Heart	4.080	0.275	6.326	0.128	726.9
Left Kidney	1.430	0.465	1.200	0.063	168.7
Right Kidney	1.357	0.449	1.501	0.106	158.8
Liver	14.708	0.509	18.410	0.154	1670.3
Left Lung	4.404	0.032	38.230	0.465	2110.9
Right Lung	5.922	0.046	43.438	0.475	2335.5
Pancreas	0.699	0.167	1.075	0.076	93.3
Spleen	2.247	0.267	5.141	0.271	204.2
Stomach	0.335	0.005	2.628	0.065	253.7
Thymus*	0.040	0.089	0.205	0.441	22.9
Thyroid	0.030	0.117	0.118	0.358	20.5

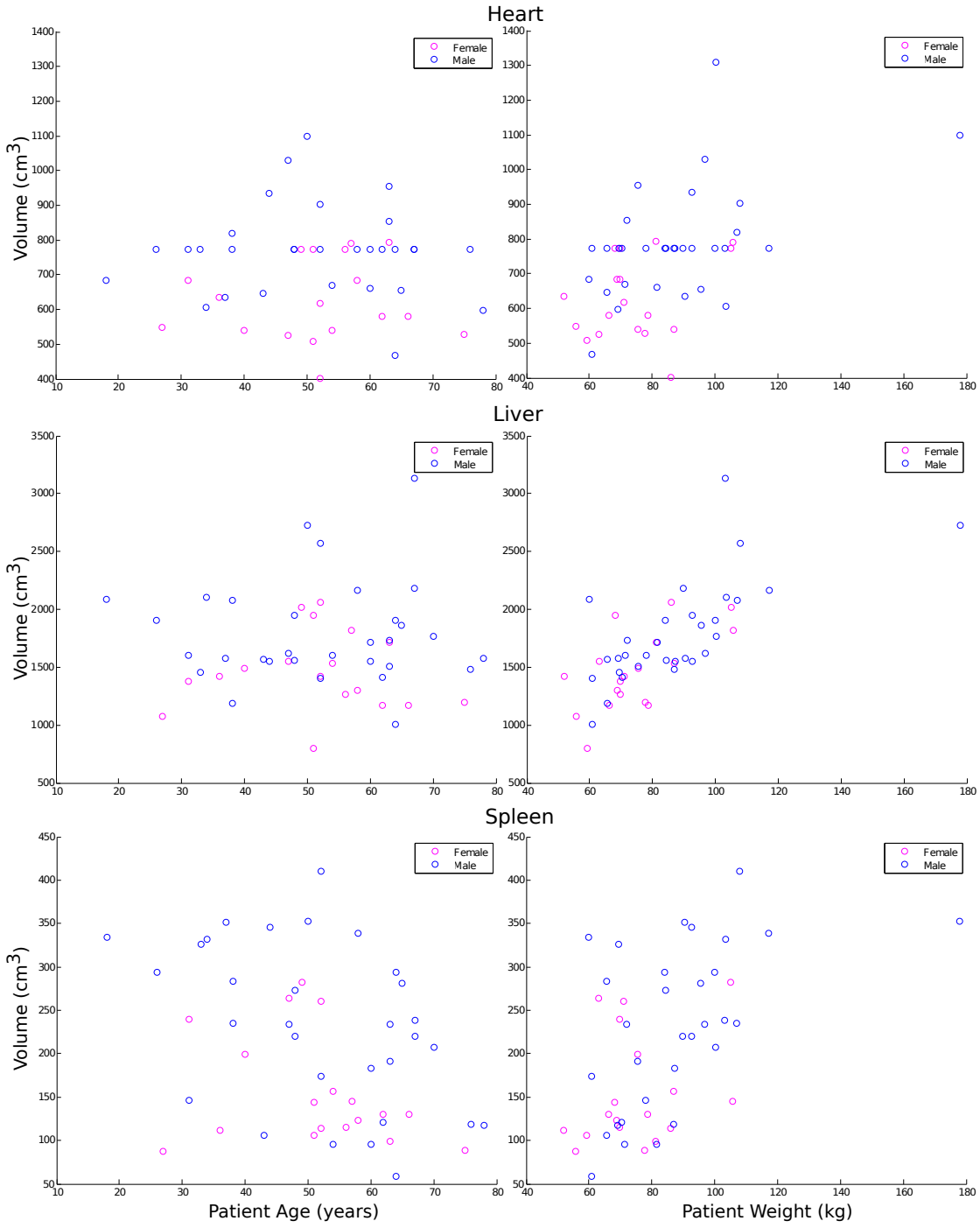

Figure 12: Adult organ volumes plotted versus age (left column) and weight (right column). Weight demonstrates a positive, linear relation while age shows little correlation with volume.

3.2 Pediatrics

The pediatric models were created from a wide distribution of ages ranging from 5 weeks to 15 years. Unlike adult organs which are virtually static, pediatric organs develop rapidly from infanthood into adolescence. The organ midpoints, axial widths, and volumes were tracked as functions of patient age with various fits performed.

3.2.1 Axial Midpoint

The axial midpoints show a clear cube root relation to pediatric patient age (mean $r^2 = 0.790$). In Table 6, the r^2-values for the cube root fits exceed the corresponding linear and log fits. The LDDMM transformed organs (i.e. adrenals, thymus, and thyroid) show the same behavior as the manually segmented organs. Figure 13 displays the plots for the heart and the liver. The males and females were fitted separately with the intent to characterize different behaviors between genders; however, the noise in the relatively few number of data points degrades the quality of the fits.

Table 6: r^2-values for linear, log, and cube root fits performed on pediatric axial midpoints as a function of age. The coefficients *a* and *b* for the cube root functions are also shown. Organs that were not manually segmented are marked with an asterisk.

Organ	Linear	Log	Cube Root	*a* (Cube Root)	*b* (Cube Root)
Left Adrenal*	0.757	0.765	0.817	76.8	69.7
Right Adrenal*	0.737	0.766	0.811	76.0	64.7
Gall Bladder	0.581	0.679	0.686	60.3	76.0
Heart	0.758	0.818	0.849	101.9	117.5
Left Kidney	0.717	0.729	0.779	67.9	60.5
Right Kidney	0.694	0.720	0.766	67.9	55.7
Liver	0.651	0.738	0.751	67.4	82.5

Left Lung	0.781	0.810	0.857	108.2	113.6
Right Lung	0.769	0.800	0.845	109.6	111.8
Pancreas*	0.589	0.667	0.677	61.2	70.0
Spleen	0.720	0.774	0.809	75.6	83.4
Stomach	0.601	0.699	0.706	76.1	80.4
Thymus*	0.760	0.806	0.845	117.0	134.5
Thyroid*	0.775	0.808	0.857	129.6	147.5

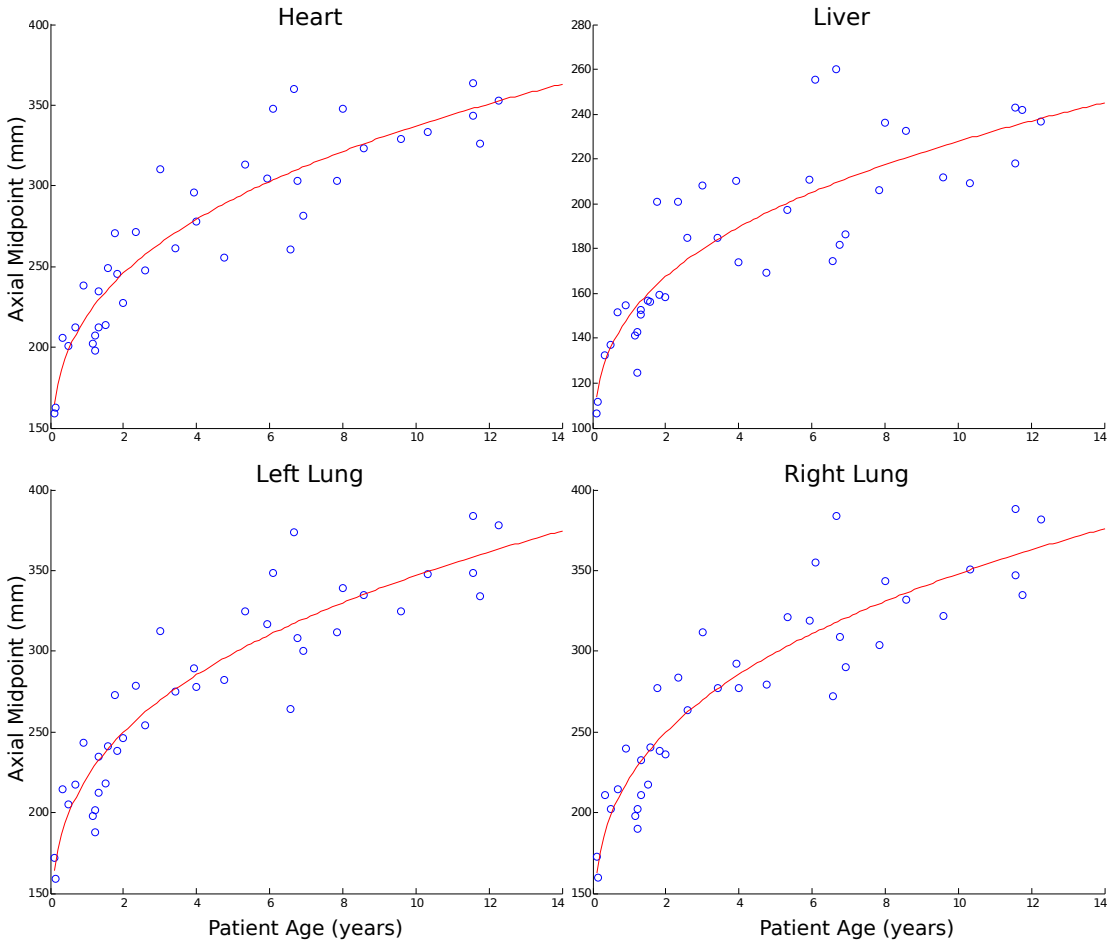

Figure 13: Pediatric axial midpoints of the heart, liver, and lungs plotted as functions of age. The organs are shown with cube root fits (red).

3.2.2 Axial Widths

The axial widths plotted as functions of patient age demonstrate stronger correlations to cube root fits (mean $r^2 = 0.564$) than either linear or logarithmic fits. This can be seen in Table 7 where the linear r^2-values are greater than the cube root values. The thyroid and stomach did not follow the overall trend, showing better correlation with linear functions. The genders were fitted separately, but again the limited number of data points weakens the statistical significance of the fits.

Table 7: r^2-values for linear, log, and cube root fits performed on pediatric axial widths plotted versus age. The coefficients *a* and *b* for the cube root fits are also shown. Organs that were not manually segmented are marked with an asterisk.

Organ	Linear	Log	Cube Root	*a* (Cube Root)	*b* (Cube Root)
Left Adrenal*	0.445	0.239	0.338	5.39	29.81
Right Adrenal*	0.455	0.154	0.275	3.22	30.29
Gall Bladder	0.314	0.285	0.319	17.04	9.35
Heart	0.762	0.710	0.784	38.25	27.50
Left Kidney	0.621	0.577	0.628	24.61	32.96
Right Kidney	0.613	0.599	0.637	23.38	31.72
Liver	0.625	0.656	0.682	47.44	38.96
Left Lung	0.753	0.658	0.750	57.69	42.86
Right Lung	0.766	0.657	0.757	59.16	44.70
Pancreas*	0.559	0.587	0.608	17.62	20.63
Spleen	0.590	0.576	0.613	34.61	9.04
Stomach	0.506	0.400	0.463	30.33	12.81
Thymus*	0.083	0.172	0.138	4.39	36.38
Thyroid*	0.986	0.761	0.905	9.58	9.69

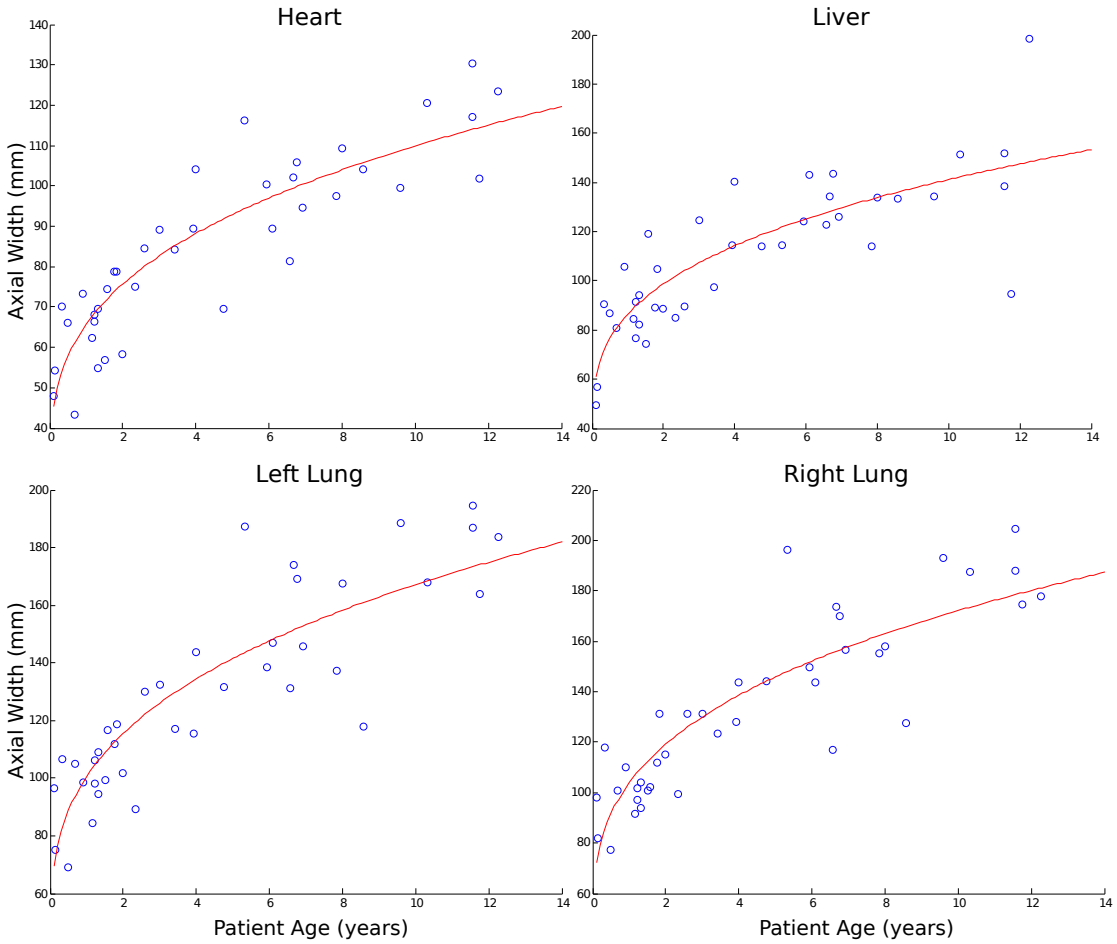

Figure 14: Pediatric axial widths of the heart, liver, and lungs plotted as a function of age. Cube root fits are shown in red.

3.2.3 Organ Volumes

The pediatric midpoints and widths were found to be best fitted by cube root functions. Since $age \propto width^3$ and $volume \propto width^3$, it follows that volume should be linearly related to age. The volumes, therefore, were fitted with linear functions. The results are summarized in Table 8. Logarithmic fits were also performed for comparison. Most manually segmented organs follow a positive, linear trend (mean r^2 =

0.701) with the exception of the kidneys which show slight improvement as logarithms. The logarithmic r^2-value of the thymus is significantly larger than the corresponding linear r^2-value.

Table 8: r^2-values for log and linear fits on pediatric organ volumes as a function of age. The slopes (m) and y-intercepts (b) of the linear fits are also given. Organs that were not manually segmented are marked with an asterisk.

Organ	Log	Linear	m (Linear)	b (Linear)
Left Adrenal*	0.309	0.698	0.189	2.08
Right Adrenal*	0.215	0.522	0.126	2.13
Gall Bladder	0.438	0.642	2.16	3.90
Heart	0.708	0.771	28.34	94.61
Left Kidney	0.666	0.640	6.25	35.75
Right Kidney	0.661	0.661	5.94	33.68
Liver	0.773	0.783	62.01	275.87
Left Lung	0.642	0.809	69.91	117.36
Right Lung	0.652	0.804	77.37	147.23
Pancreas*	0.732	0.983	5.60	11.76
Spleen	0.621	0.640	11.15	33.72
Stomach	0.431	0.448	13.11	68.38
Thymus*	0.793	0.433	0.772	26.76
Thyroid*	0.648	0.978	0.718	0.860

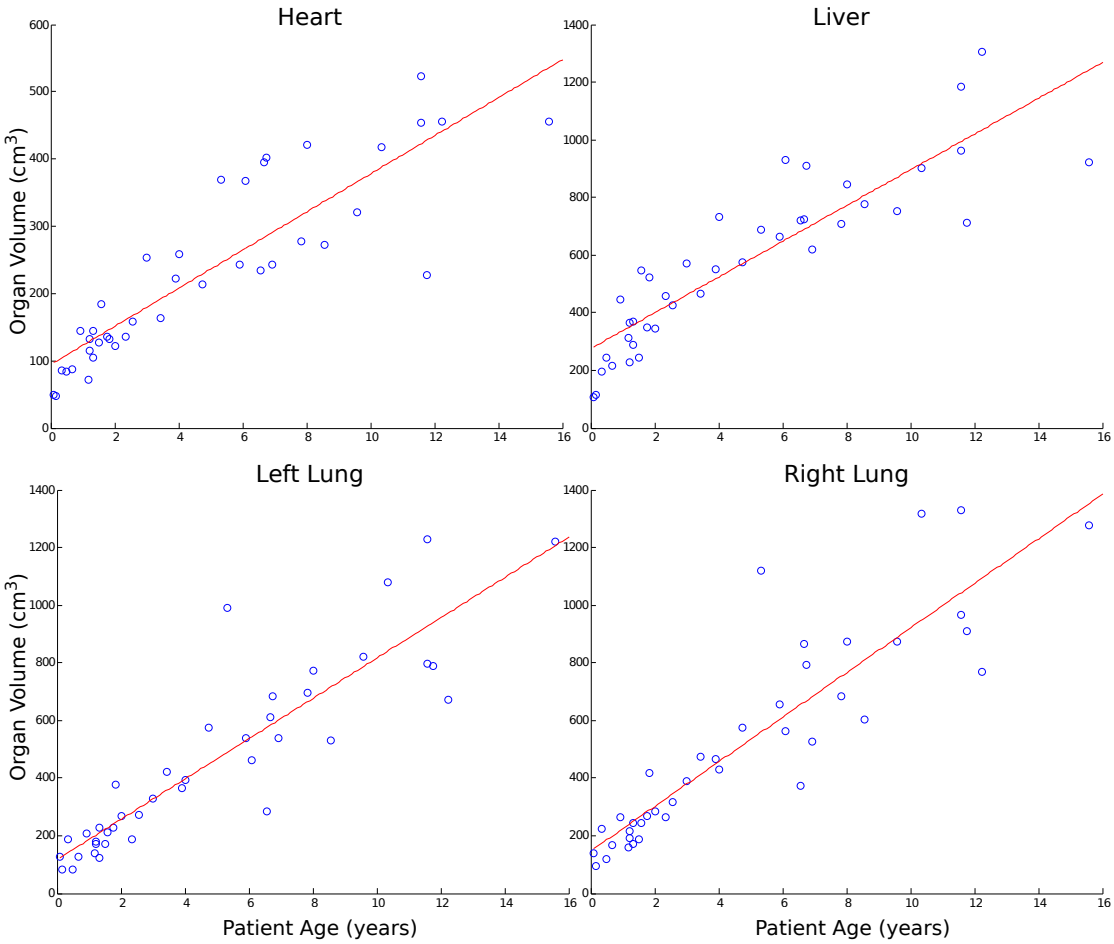

Figure 15: Pediatric volumes of the heart, liver, and lungs plotted as a function of age. Linear trend lines are drawn in red.

4. Discussion

The patient specific XCAT models used throughout this work allow us to study organ volumes and locations with unparalleled sophistication and detail. Because the XCAT phantoms are constructed from manually segmented structures from patient data, our methods are based on real patient anatomy instead of generic phantoms. The existing works in the field of organ volumetry only examine the spleen, liver, and kidneys for diagnostic purposes. These diagnostic aims place no emphasis on organ location, leaving a void in the anatomical information available for applications to dosimetry.

4.1 Adults

For the adult population, axial midpoints, widths, and volumes have no significant correlation with patient age or BMI. There is a weak, positive linear relationship between these parameters and patient weight and height. The lung parameters most highly correlate with height, while the heart midpoint and volume correlate highly with patient weight. Comparing our splenic volume (204.2 cm^3) to published data from *Prassopoulos et al.* indicates an error of 4%. We find this acceptable since our CT images used higher axial resolution (5mm vs. 10mm) and the range of normality extends from 107.2 to 314.5 cm^3 [22]. A total of 8 out of our 51 patients had splenic volumes that exceeded the nominal upper limit. Of these 8 patients, 6 of them had body weights exceeding 200 lbs. Since our patients were screened for any

pathologies affecting organ morphology, physicians should take patient weight into account when assessing normal splenic volumes.

In general, heavier patients will have larger organs, and these organs will be located farther away from the sacrum (as defined by axial midpoint). These deviations, however, are small relative to overall organ size, leading us to consider the adult population as a single cohort. With 51 adults in our cohort, we were able to generate probability density functions for each organ.

Figures 9-11 demonstrate the highly Gaussian nature of these PDFs. The goodness of fit is confirmed by the r^2-values in Table 4. All organs, excluding the manually fitted ones, have r^2-values in excess of 0.97. The manually fitted left and right lungs deviate more significantly from the PDFs than the other organs. This was expected since a ceiling was placed on the Gaussian amplitude to prevent the normalized frequency from exceeding 1.0. Because of this, the tails of the Gaussians extend beyond the edges of the PDFs. We find it acceptable to overestimate our confidence interval to encompass all the patients in the cohort.

The normal distribution statistics associated with Gaussian functions give us a powerful tool for predicting organ location. As more adult patients are added to the population, the jagged edges of all PDFs should smooth out and reinforce the statistical power of these methods. Similar methodology can be applied to sagittal and coronal

axes. 95% confidence intervals for all three coordinate axes can be calculated to serve as the dimensions of the rectangular confidence volume as seen in Figure 6.

With the mean volumes calculated and displayed in Table 5, an organ characterized by average volume and typical morphology can be placed within the 95% confidence volume for dose calculations. It is important to note that even though we've shown that organ volume and location with respect to bony anatomy does not vary greatly with adult patient age, height, and weight, this does not mean all adult patients will receive the same organ dose irrespective of patient parameters. On the contrary, the amount of adipose tissue enveloping the bone structure significantly affects organ dose. To this end, it is important to continue expand the library of XCAT phantoms to build a more extensive catalog of patient anatomies.

4.2 Pediatrics

There are significant variations in organ midpoint, width, and volume within the pediatric population as the organs develop to maturity with age. Because of the dynamic nature of their organs, pediatrics should not be treated as a single cohort with probability density functions as in the adult models. Unlike the adults, the variation in organ parameters is substantial relative to the overall size of the organs. The axial midpoints and widths for the pediatric patients exhibited the strongest correlation with age as cube root functions. The cube root fits do tend to overestimate volume and width at young ages (between 0 and 2 years). The data can be better fit by determining the age

range at which organ development stops. Figure 16 shows a plot of heart volume versus age across both adult and pediatric patients. More data points are needed to define a range at which pediatric organs reach maturity.

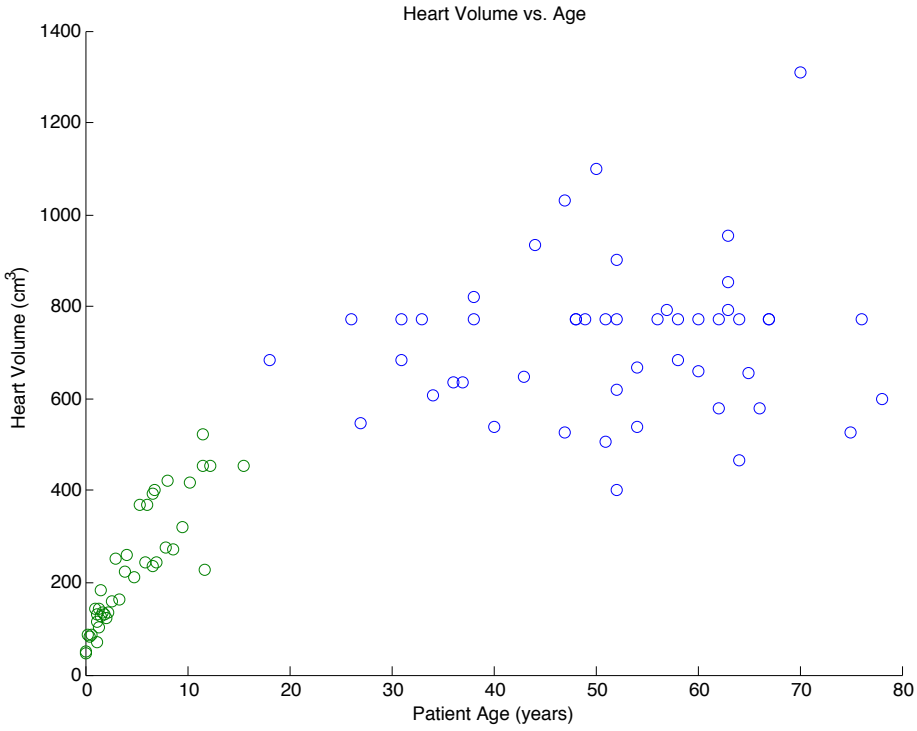

Figure 16: Heart volume plotted as a function of patient age, across both adult (blue) and pediatric (green) cohorts. More data points are needed between 10 and 20 years to define a better predictive model.

The organ volumes were found to be proportional to pediatric age. These behaviors follow logically from $volume \propto width^3$. There were irregularities occurring within these general trends. In Table 7, the stomach and thyroid show stronger correlation with linear fits than cube root fits. The thyroid was the only LDDMM transformed organ that did not behave the same as the manually segmented organs. This can be attributed to the fact that the heads and necks were developed in the

modeling process and not explicitly mapped from the CT data. This leads to a significant departure from the cube root trend. The stomach, however, was manually segmented in the pediatric patients. Further adjustments should be made to our modeling of pediatrics to account for the overtly linear scaling of the thyroid and thymus. Despite the stomachs behaving "well" in the adult models, the pediatric stomach widths and volumes did not. Since the stomach volume and position can vary greatly depending on how much food was consumed prior to the scan, our conjecture is that the pediatrics did not strictly adhere to the pre-scanning protocols.

Because of the considerable growth of pediatric organs, the analysis done in this study would benefit from a larger number of pediatric models. More patients in the age range of 0-4 years where the cube root function is most rapidly changing would be the most beneficial to the modeling process. The results thus far, however, are very promising when considering the significantly higher r^2 values of the pediatrics versus those of the adults.

4.3 Conclusion and Future Studies

While we have conducted a first order analysis of organ size and location with respect the axial direction, similar analyses should be done to incorporate the sagittal and coronal axes. This will yield a more complete localization of patient organs. The next step is to apply this information to organ dosimetry. The radial and axial x-ray tube current modulations are currently available for clinical CT scanners. By combining

this information with the predictive models of organ location and size developed in this study, prospective organ dosimetry is achievable.

While the three major patient axes were used in this project, a more nuanced study of a particular organ can be conducted using organ specific axes to chart organ development. For example, axial widths with respect to the long and short axes of the heart may be a better approximation for organ size. Correlating PET and CT organ data is another avenue to pursue.

Recently, Monte Carlo models of CT examinations of have been successfully developed and validated in our institution [23]. These Monte Carlo models have been applied to a small number of pediatric XCAT phantoms for organ dose estimation [24]. The ultimate goal is to generate a total of 400 XCAT phantoms, equally distributed between adults and pediatrics across a variety of anatomies, and subsequently calculate organ doses for the phantom population. A patient coming in for a particular CT examination can then be matched to a model.

This organ localization study can aid in the process of model selection. While the XCAT population will span across a variety of ages, heights, and weights, the phantoms themselves are representative of the patients from which the anatomy was manually segmented and not necessarily the patient coming in for the CT exam. We want to be able to select the model that has the highest probability of matching the anatomy of the individual. With an understanding of how organ volumes and locations are distributed

within the XCAT population, certain outliers can be identified and a proper phantom can be chosen. Also, while building our library, adult ages should be neglected in favor of body habitus since organ development stops in adulthood.

References

1. AAPM, "Staffing Levels and Responsibilities of Physicists in Diagnostic Radiology," AAPM Publication 33 (American Association of Physicists in Medicine).

2. Brody, A. S., D. P. Frush, W. Huda, and R. L. Brent, "Radiation Risk to Children from Computed Tomography," Pediatrics **120**, 677-682 (2007).

3. NCRP, "Ionizing Radiation Exposure of the Population of the United States," NCRP Publication 160 (National Council of Radiation Protection and Measurements).

4. Zarembo, A. (2009, October 16). "Hospital error leads to 206 radiation overdoses; Stroke patients were given 8 times the normal dose during brain scan procedures, Cedar-Sinai says," *Los Angeles Times*. Retrieved February 15, 2012 from http://www.latimes.com.

5. Richwine, L. (2009, December 7). "U.S. probing more cases of CT radiation exposure," *Reuters.* Retrieved February 15, 2012 from http://www.reuters.com.

6. ACR, "Summary of the California Senate Bill 1237," American College of Radiology. Retrieved February 15, 2012 from http://www.acr.org.

7. AAPM, "Standardized Methods for Measuring Diagnostic X-Ray Exposures," AAPM Publication 31 (American Association of Physicists in Medicine).

8. AAPM, "The Measurement, Reporting, and Management of Radiation Dose in CT," AAPM Publication 96 (American Association of Physicists in Medicine).

9. AAPM, "Comprehensive Methodology for the Evaluation of Radiation Dose in X-Ray Computed Tomography," AAPM Publication 111 (American Association of Physicists in Medicine).

10. AAPM, "Size Specific Dose Estimates (SSDE) in Pediatric and Adult Body CT Examinations," AAPM Publication 204, (American Association of Physicists in Medicine).

11. Zhang, D., et al., "Variability of surface and center position radiation dose in MDCT: Monte Carlo simulations using CTDI and anthropomorphic phantoms," Med Phys **36** (3), 1025-1038 (2009).

12. Zhou, H. and J. M. Boone, "Monte Carlo evaluation of $CTDI_{inf}$ in infinitely long cylinders of water, polyethylene and PMMA with diameters from 10 mm to 500 mm," Med Phys **30** (6), 2424-2431 (2008).

13. Li, X., E. Samei, W.P Segars, G. M. Sturgeon, J. G. Colsher, and D. P. Frush, "Patient-specific Radiation Dose and Cancer Risk for Pediatric Chest CT," Radiology **259** (3), 862-874 (2011).

14. Brieman, R. S., J. W. Beck, M. Korobkin, R. Glenny, O. E. Akwari, D. K. Heaston, A. V. Moore, and P. C. Ram, "Volume Determinations Using Computed Tomography," Am J Roentgenol **138**, 329-333 (1982).

15. Yetter, E. M., K. B. Acosta, M. C. Olson, and K. Blundell, "Estimating Splenic Volume: Sonographic Measurements Correlated with Helical CT Determination," Am J Roentgenol **181,** 1615-1620 (2003).

16. Asghar, A., D. Agrawal, S. M. Yunus, P. K. Sharma, S. H. Zaidi, and A. Sinha, "Standard Splenic Volume Estimation in North Indian Adult Populations: Using 3D Reconstruction of Abdominal CT Scan Images," Anatomy Research International (2011).

17. Konus, O. L., A. Ozdemir, A. Akkaya, G. Erbas, H. Celik, and S. Isik, "Normal liver, spleen, and kidney dimensions in neonates, infants, and children: evaluation with sonography," Am J Roentgenol **171** (6), 1693-1698 (1998).

18. Suzuki, K., M. L. Epstein, R. Kohlbrenner, S. Garg, M. Hori, A. Oto, and R. L. Baron, "Quantitative Radiology: Automated CT Liver Volumetry Compared with Interactive Volumetry and Manual Volumetry," Am J Roentgenol **197**, 706-712 (2011).

19. Cody, D. D., D. M. Moxley, K. T. Krugh, J. C. O'Daniel, L. K. Wagner, and F. Eftekhari, "Strategies for Formulating Appropriate MDCT Techniques When Imaging the Chest, Abdomen, and Pelvis in Pediatric Patients," Am J Roentgenol **182**, 849-859 (2004).

20. Segars, W. P., et al., "Patient Specific Computerized Phantoms to Estimate Dose in Pediatric CT," Proceedings of the SPIE **7258**, pp. 72580H-72580H-9 (2009).

21. Beg, M. F., M. I. Miller, A. Trouve, and L. Younes, "Computing Large Deformation Metric Mappings via Geodesic Flows of Diffeomorphisms," International Journal of Computer Vision **61** (2), 139-157 (2005).

22. Prassopoulos, P., et al., "Determination of normal splenic volume on computed tomography in relation to age, gender, and body habitus," Eur Radiol **7**, 246-248 (1997).

23. Li, X., et al., "Patient-specific radiation dose and cancer risk estimation in CT: Part I. Development and validation of a Monte Carlo program," Med Phys **38** (1), 397-407 (2011).

24. Li, X., et al., "Patient-specific radiation dose and cancer risk estimation in CT: Part II. Application to patients," Med Phys **38** (1), 408-149 (2011).